Full Paper
Journal of Nano Materials Impact 2026, 02 (02) 11-22

Effect of Plasma Properties on The Structure of The Zinc Surface Via Microwave Plasma

Heba G. Akhlefa, Baida M. Ahmed*
Department of Chemistry, College of Science, Mustansiriyah University, 10052 Baghdad, Iraq.

Abstract

Study the effect of different gas ratios (argon/oxygen) using microwave plasma and optical emission spectroscopy (OES) on the surface properties of zinc (Zn). The effects of electron temperature and resulting electron density on the etching of the zinc surface were examined at three plasma voltages (50, 100, and 150 V) and at a frequency of 2.45 GHz. Additionally. The Boltzmann plot method provides an effective means to determine the electron temperature in plasma and to study its behavior under different operating conditions for various gas ratios (Ar 100%, Ar 20% - O 80%, and Ar 80% - O 20%) of (4.2, 2.16, and 0.59 eV), respectively. The Stark broadening method provides electron density for the same ratio gases (9.9, 8.4, and 9.26) $\times 10^{17}$ cm^{-3}, respectively. The X-ray diffraction (XRD) pattern shows peaks between 40° and 50°, indicating the formation of a densely packed hexagonal structure of zinc and zincite. Field emission scanning electron microscopy (FE-SEM) images revealed the effect of argon gas concentration on zinc surface etching. The images showed that the zinc surface was most affected at a 100% argon concentration, and the effect decreased with increasing oxygen concentration, until the surface became smoothest at an 80% oxygen concentration.

Keyword: Zn foil nanostructure • microwave plasma • plasma spectral • Ar and O gases.

Downloaded from https://nanomatimp.uomustansiriyah.edu.iq/

Introduction

Plasma is considered one of the fundamental physical states of matter. It's an ionized gas composed of free electrons, ions, and neutral particles[1-4], characterized by its ability to exhibit collective behavior due to electromagnetic interactions among its components[5, 6]. As the temperature of a substance increases, it transitions from the solid state to the liquid and then to the gaseous state, and with continued heating to higher levels[7-9], ionization of the gas occurs, leading to the formation of plasma, which is known as the fourth state of matter[10-12]. Based on the thermal equilibrium among its components[13], plasma is classified into thermal equilibrium plasma (TP) and non-thermal equilibrium plasma (NTP)[14, 15]. In the first case, the temperatures of electrons and ions are equal and reach very high values[16, 17], whereas non-thermal plasma is characterized by the low temperature of heavy particles compared to electrons[18-20].Microwave plasma is considered one of the most advanced types of plasma due to its ability to generate stable plasma with high density without the need for direct electrodes[21, 22], which reduces contamination and improves the uniformity of processing[23].

***Address for correspondence:** Prof. Dr. Baida M. Ahmed, Department of Chemistry, College of Science, Mustansiriyah University, 10052 Baghdad, Iraq.
E-mail: dr.baida_222@uomustansiriyah.edu.iq
ORCID: https://orcid.org/0000-0001-9315-1913

This is an open-access journal, and articles are distributed under the terms of the Creative Commons Attribution License (CC-BY) 4.0 License, which allows others to use, distribute, and reproduce in any medium for noncommercial purposes, as long as the original work is cited properly.

Info:
Submitted: 13 June 2026; **Revised:** 11 July 2026;
Accepted: 01 Aug. 2026; **Published:** 15 Aug. 2026.
https://doi.org/10.71109/nmi.2026.2.2.29

This technology also provides precise control over plasma properties by adjusting operating parameters such as power[24, 25], pressure[26], and the type and ratio of gases used[27].

The gas mixture of argon and oxygen (Ar/O_2) is considered one of the most commonly used systems[28], as argon plays a fundamental role in maintaining the stability of the plasma discharge and increasing electron density due to its low ionization energy[29, 30], While oxygen contributes to the generation of reactive oxygen species (ROS), which enhance surface interactions and lead to increased surface roughness and surface energy and improve wettability, as well as promoting the formation of an oxide layer and increasing corrosion resistance and biocompatibility of the material[31, 32], particularly in applications related to corrosion resistance and biocompatibility[33]. Changing the gas ratios in (Ar/O_2) plasma leads to fundamental changes in the plasma properties[28], particularly in the distribution of electron energy[34], the density of active species[35], and the interaction behavior with the surface[36]. Argon gas (Ar) is widely used as an inert gas due to its ability to facilitate the plasma evacuation process and increase electron density. The active particles generated in the plasma also contribute to modifying the surface morphology and structure, Active argon ions interact with the material surface through ion bombardment, leading to surface etching, atomic rearrangement, and the formation of new active sites, thus changing the surface properties and morphology. which affects the material's properties and various applications[37, 38], which play a key role in modifying the surface properties of materials[39], including energy distribution[40], electron density[41], electron temperature (Te)[42], as well as the nature of the active species formed within the plasma[43]. Therefore, understanding the

Copyright © 2026. This work licensed under a Creative Commons Attribution Noncommercial 4.0 International License.

relationship between gas ratio and plasma properties is essential for improving surface process performance and controlling the microstructure of treated materials[44, 45].

Theoretical Section

Optical Emission Spectroscopy (OES) is considered one of the most important plasma diagnostic techniques[46], due to its non-intrusive nature that allows for the analysis of emitted radiation over a wide range of wavelengths (200–800 nm)[47]. By analyzing the intensity of the spectral lines of the excited species[48], the qualitative composition of the plasma can be determined[49], and the excitation and ionization mechanisms can be understood[50]. The Boltzmann plot method can also be used to extract the electron temperature[51], which is one of the most important physical parameters reflecting the energy distribution within the plasma[52]. The electron temperature is defined under LTE condition as follows[53]:

$$\ln\left[\frac{\lambda_{ji}\, I_{ji}}{h\, C\, A_{ji} g_j}\right] = \left(-\frac{E_j}{K_{T_e}}\right) + \ln\left|\frac{N}{U(T)}\right| \quad \text{... (1)}$$

where (λ_{ji}) wavelength correspondent the transmission between two levels, (I_{ji}) spectral line intensity, (A_{ji}) transition probability between two levels, (E_j) excitation energy, (g_j) the density of states, (k) Boltzmann constant, U(T) is the partition function, and (N) total population density.

Furthermore, the significance of this technique lies in its ability to extract fundamental plasma parameters such as the electron temperature (Te) and electron density (ne)[54], as (Te) can be calculated using Boltzmann plots based on the intensity of spectral lines[55], while (ne) is determined through the analysis of Stark broadening of spectral lines using the full width at half maximum (FWHM) value[56]. The Stark broadening, which applies exclusively to high-density plasma, is given by[57]:

$$n_e(CM^{-3}) = \left(\frac{\Delta\lambda}{2W_s\left(\lambda,\ Te\right)}\right) N_r \quad \text{... (2)}$$

The stability of charge neutrality in the bulk region is a fundamental feature of plasma. When the plasma is subjected to a sudden disturbance from its equilibrium state, a strong electric field is generated, stimulating collective motions of the particles that act to restore the initial charge neutrality[58]. These motions are characterized by the plasma frequency, which is an internal oscillation frequency defined as follows:

$$f_p = \sqrt{\frac{n_e\, e^2}{m_e\ \ \epsilon_\circ}} = 8.89\sqrt{n_e} \quad \text{... (3)}$$

The Debye plasma length is another physical measure used to characterize plasma. It helps in measuring the distance between electrons and ions in the plasma. The arrangement between electrons and ions is effectively reduced by electrostatic forces at a distance determined by the Debye plasma length (λ_D), as shown in[59]:

$$\lambda_D = \sqrt{\frac{\varepsilon_\circ\ \ K_B\ T}{n_e\ \ e^2}} \quad \text{... (4)}$$

In plasma physics, charged particles within a Debye sphere interact only collectively; hence, the number of electrons (ND) within a Debye sphere is expressed as follows[57]:

$$N_D = \frac{4}{3}\pi\ \lambda_D^3\ n_e \quad \text{... (5)}$$

On the other hand, plasma treatment plays an important role in improving surface properties such as roughness, surface energy, and chemical reactivity[58]. A field emission scanning electron microscope (FE-SEM) is used to study the morphological changes resulting from plasma treatment with high precision[59], providing a deep understanding of the relationship between plasma properties and surface structure[60].

Microwave plasma was used at a frequency of (2.45 GHz) and an operating power of (1000 W), with varying ratios of argon and oxygen gas mixture, and standard spectral data extracted from the NIST database were relied upon to identify and analyze the emission lines used in the study of the spectral properties of the resulting plasma[61], to study their effect on the spectral properties of the plasma using the OES technique, in addition to calculating the electron temperature and density on the zinc foil[62].

The study aims to investigate the impact of changing the ratios of argon and oxygen gases in microplasma on the spectral properties and plasma parameters, particularly the electron temperature and density, using the (OES) technique. In addition, it examines the effect of these changes on the surface structure of zinc metal using (FE-SEM), through which the morphological changes of the zinc surface were analyzed with the aim of correlating plasma properties with the improvements occurring in the surface structure.

Experimental Section

Figure 1, illustrate the system of microwave plasma. A plasma microwave system has been designed to operate at a variable frequency and voltage (2.45 GHz) (0 to 200) volts respectively. It includes a magnetron connected to a waveguide to enhance the density of the electromagnetic wave, in addition to fibers and an optical emission spectroscopy (OES) device (Ocean Optics Spectrometer, Flame-S-XR1). The spectrum appeared on the computer screen as peaks resulting from the optical emission spectroscopy (OES) measurements, compared with the NIST atomic spectral database[63]. The surface area of each zinc piece (length × width) was 1 cm^2, with a thickness of (0.25 mm). They were cleaned using ethanol and distilled water in an ultrasonic device for (15 minutes) to remove any impurities on the zinc sheets and then left to air dry. The zinc foils were exposed to microwave input voltage of (50, 100, and 150) volts to study the plasma spectra and its parameters**.** The microwave plasma system was operated under atmospheric pressure conditions. A total gas flow rate of 20 liters/minute was maintained using a flowmeter for each of the mixed gas compositions. Plasma was generated using a quartz tube nozzle with a length of 30 cm, an inner diameter of 5 mm, and an outer diameter of 7 mm. An approximately 1.5 cm visible plasma cloud was observed at the nozzle exit,

Downloaded from https://nanomatimp.uomustansiriyah.edu.iq/

Copyright © 2026. This work licensed under a Creative Commons Attribution Noncommercial 4.0 International License.

characterized by a light purple emission. Zinc samples were placed directly under the plasma jet at a fixed distance of 1 cm to ensure direct exposure to the active plasma region.

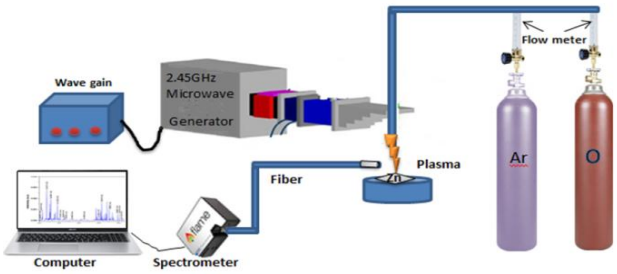


Figure 1. Schematic diagram of the (Ar/O_2) Microwave plasma system.

Results and Discussion

Optical Emission Spectrum (OES)

Figure 2 shows the atomic emission spectra of plasma on the zinc surface at three applied voltages (50, 100, and 150 volts), where the spectrum is analyzed and plasma parameters are calculated based on Optical Emission Spectroscopy (OES) to study the effect of gas ratios on plasma properties. The plasma spectrum in the figures illustrated, that the intensity of the spectral lines of argon and oxygen gases depends greatly and directly on the gas ratio in the plasma mixture. When the argon ratio is 100%, notice the active role of electrons in exciting argon atoms. However, when the oxygen ratio is 80%, the increase in the density of active particles causes the oxygen spectral lines to become clearly visible, in addition to energy transfer from excited argon atoms to oxygen molecules, which enhances their spectral emissions. Moreover, collision and dissociation processes in oxygen consume plasma energy, reducing the intensity of argon emission and increasing the dominance of oxygen in the spectrum. When zinc metal is exposed to pure argon and oxygen ratios, it directly affects the surface of zinc due to several factors. First, excitation, emission, and the appearance of zinc spectral lines. Second, surface sputtering, where positive argon ions (Ar^+) work to excite zinc atoms and eject them. Third the oxidation oxygen, where reacts with zinc to form ($O_2 + e^- \rightarrow 2e$). Therefore, we observe stable plasma with high electron density and no chemical reactions. And since argon is heavy, it transfers high momentum. In the case of an argon ratio of 80%, the percentage of energy that argon provides to the plasma is high. Oxygen breaks and reacts with zinc ($Zn + O \rightarrow ZnO$).

The changes in plasma properties with varying Ar/O_2 ratios can be explained based on the different physical characteristics and reaction mechanisms of argon and oxygen in the plasma. Argon, being a noble gas, is characterized by efficient electron excitation and ionization processes, enhancing the production of active electrons and maintaining a relatively high electron density. With an increase in the oxygen ratio, oxygen molecules act as negatively charged species that capture free electrons through electron attachment processes, leading to a reduction in electron densityIn addition, part of the electron's energy is consumed in the dissociation and excitation of oxygen molecules, which can alter the distribution of electron energy and affect the electron temperature. The transfer of energy from excited argon atoms to oxygen species further enhances oxygen-related emission lines, while reducing the relative intensity of argon emissions. Therefore, the Ar/O_2 ratio plays a crucial role in determining plasma stability, electron dynamics, and optical emission behavior.

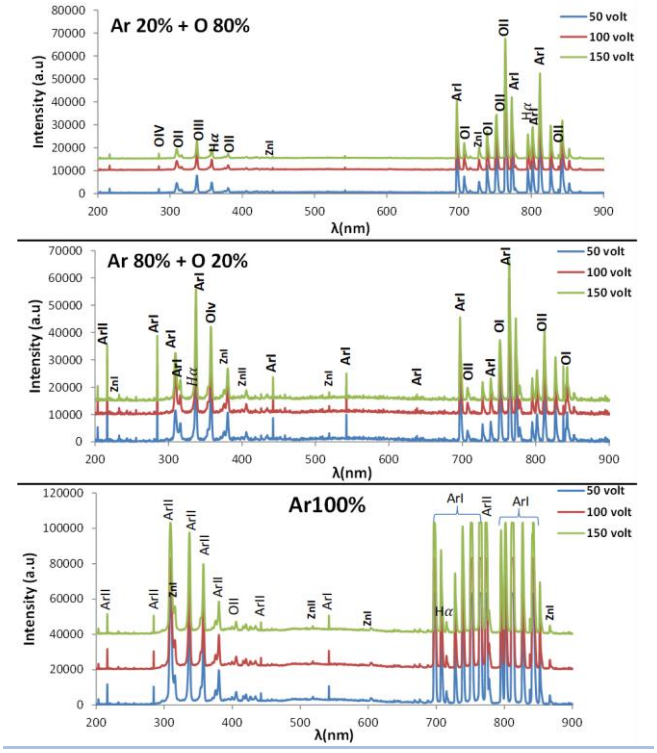


Figure 2. Emission spectrum spectroscopy of zinc at different voltages (50, 100, and 150 volts) and different gas ratios using microwave plasma.

Tables (1, 2, and 3) illustrate the prominent emissions and plasma energy spectrum of oxygen and argon on the zinc surface. The highest and most prominent peaks for oxygen, argon, and zinc are presented (OI represents the first ionization, OII the second ionization, and OIII and OIV for oxygen), (ArI the first ionization, ArII the second ionization), (ZnI the first ionization, ZnII the second ionization), along with the lowest and highest energy levels, and the transition energy at different voltages (50, 100, and 150 volts) in **Table 3**. The spectral emission was correlated with NIST data.

Downloaded from https://nanomatimp.uomustansiriyah.edu.iq/

Copyright © 2026. This work licensed under a Creative Commons Attribution Noncommercial 4.0 International License.

Table 1. Spectral data on the emission lines of the Argon and Oxygen ratio (Ar20% and O80%), wave length, Intensity, the lower and upper energy levels, and energy transition levels at different voltages (50, 100, and 150) volts.

Ion	λ (nm)	I(a.u)	Ak.i	E2(ev)	Transition lower energy levels	Transition upper energy levels
O III	268.5	336.64	1.84e+08	49.650	2s2p2(4P)3p	2s 2p^{s} (^{4}p^{0})3d
O IV	307.77	6605.29	1.29e+08	48.373	2s23s	2s23p
O II	336.3	20420.7	6.89e+07	32.519	2s22p2(3P)3d	2s22p2(3P)5p
O III	369.1	15518.44	7.76e+07	48.698	2s22p2(2P°)4p	2s22p(2P°)5s
O II	432.11	10638.16	1.11e+04	31.756	2s22p2(3P)3d	2s22p2(3P)4f
O II	494.06	15548.27	7.88e+07	29.068	2s22p2(3P)3p	2s22p2(3P)3d
O II	727.17	19805.36	7.17e+05	30.560	2s22p2(3P)3d	2s22p2(3P)4p
O II	738.3	6054.73	4.73e+05	30.536	2s22p2(3P)3d	2s22p2(3P)4p
O I	753.9	5667.04	6.91e+05	30.503	2s22p2(3P)3d	2s22p2(3P)4p
O II	762.6	17798.68	1.16e+06	30.477	2s22p2(3P)3d	2s22p2(3P)4p
O II	765.8	37706.01	2.30e+06	30.471	2s22p2(3P)3d	2s22p2(3P)4p
Ar ll	336.3	89280.57	4.1e+07	23.548	3s^{2}3p^4(^{3}P)4p	3s^{2}3p^4(^{3}P)4d
Ar ll	357.7	72073.28	5.1e+05	24.964	3s^{2}3p^4(^{1}D)4p	3s^{2}3p^4(^{3}P)5d
Ar ll	379.82	16669.78	1.7e+07	22.811	3s^{2}3p^4(^{3}P)4p	3s^{2}3p^4(^{3}P)4d
Ar ll	432.55	23685.74	5.7e+06	26.664	3s^{2}3p^4(^{1}S)4p	3s^{2}3p^4(^{1}S)5s

Table 2. Spectral data of the emission lines of Argon and Oxygen ratio (Ar80% and O20%)and zinc fronts, along with the lower and upper energy levels, in addition to the energy transition levels at different voltages (50, 100, and 150 volts).

Ion	λ (nm)	I(a.u)	Ak.i	E2(ev)	Transition lower energy levels	Transition upper energy levels
OI	753.9	5667.04	6.91e+05	30.503	2s22p2(3P)3d	2s22p2(3P)4p
OII	763.03	34904.47	1.16e+06	30.477	2s2 2p2 (3p)3d	2s2 2p2 (3p)4p
OIII	369.1	15518.44	4.01e+07	45.332	2s2 2p2(4p)3s	2s2 2p2(4p)3p
OIV	307.77	6605.29	1.29e+08	48.37382	2s2 3s	2s2 3p
ArI	696.02	100885.92	2.4e+05	14.952	3s23p5(2P°3/2)4p	3s23p5(2P°1/2)4d
ArI	826.38	21025.4	1.53e+07	13.327	3s23p5(2P°1/2)4s	3s23p5(2P°1/2)4p
ArII	750.51	9959	4.5e+07	21.624	3s23p4(3P)4p	3s23p4(1D)3d
ZnI	206.59	1035.6	4.6e+08	12.015276	3d104s	3d104p
ZnII	411.37	42246.69	8.9e+06	8.8092062	3d104s4p	3d104s6d
ZnI	531.48	10656.51	2.72e+08	6.65450963	3d104s5s	3d104s8p

Table 3. Spectral data on the emission lines of theArgon (100%) front, the lowest and highest energy levels, in addition to the energy transition levels at different voltages (50, 100, and 150) volts.

Ion	λ(nm)	I(a.u)	Ak.i	E$_2$(ev)	Transition lower energy levels	Transition upper energy levels
Arll	284.53	30508.1	2.e+05	21.498	3s^{2}3p^4(^{3}P)4s	3s^{2}3p^4(^{1}D)4p
Arll	308.22	96669.55	1.4e+08	25.444	3s^{2}3p^4(^{1}D)4p	3s^{2}3p^4(^{3}P)5d
Arll	336.3	89280.57	4.1e+07	23.548	3s^{2}3p^4(^{3}P)4p	3s^{2}3p^4(^{3}P)4d
Arll	357.7	72073.28	5.1e+05	24.964	3s^{2}3p^4(^{1}D)4p	3s^{2}3p^4(^{3}P)5d
Arll	379.82	16669.78	1.7e+07	22.811	3s^{2}3p^4(^{3}P)4p	3s^{2}3p^4(^{3}P)4d
Arll	432.55	23685.74	5.7e+06	26.664	3s^{2}3p^4(^{1}S)4p	3s^{2}3p^4(^{1}S)5s
Arl	542.1	30753.56	6.0e+05	15.362	3s^{2}3p^5(^{2}P°$_{3/2}$)4p	3s^{2}3p^5(^{2}P°$_{3/2}$)8s
Arl	696.02	100885.92	2.4e+05	14.952	3s^{2}3p^5(^{2}P°$_{3/2}$)4p	3s^{2}3p^5(^{2}P°$_{1/2}$)4d
Arl	706.23	59137.41	3.8e+06	13.302	3s^{2}3p^5(^{2}P°$_{3/2}$)4s	3s^{2}3p^5(^{2}P°$_{1/2}$)4p
Arl	727.57	74417.75	1.83e+06	13.327	3s^{2}3p^5(^{2}P°$_{3/2}$)4s	3s^{2}3p^5(^{2}P°$_{1/2}$)4p
Arl	738.77	101002.92	8.5e+06	13.302	3s^{2}3p^5(^{2}P°$_{3/2}$)4s	3s^{2}3p^5(^{2}P°$_{1/2}$)4p
Arll	750.51	9959	4.5e+07	21.624	3s^{2}3p^4(^{3}P)4p	3s^{2}3p^4(^{1}D)3d
Arl	763.5	103104.22	2.45e+07	13.171	3s^{2}3p^5(^{2}P°$_{3/2}$)4s	3s^{2}3p^5(^{2}P°$_{3/2}$)4p
Arl	826.38	21025.4	1.53e+07	13.327	3s^{2}3p^5(^{2}P°$_{1/2}$)4s	3s^{2}3p^5(^{2}P°$_{1/2}$)4p
Arl	842.54	3089.42	2.15e+07	13.0948	3s^{2}3p^5(^{2}P°$_{3/2}$)4s	3s^{2}3p^5(^{2}P°$_{3/2}$)4p

Downloaded from https://nanomatimp.uomustansiriyah.edu.iq/

Copyright © 2026. This work licensed under a Creative Commons Attribution Noncommercial 4.0 International License.

Electron Temperature (T_e)

As shown in **Figure (3, 4, and 5)**, The electron temperature (Te) was determined using the Boltzmann plot method based on selected emission lines listed in Tables (1→3).For the plasma mixture (Ar 20% – O_2 80%), the emission lines at 336.3, 357.7, 379.82, and 432.55 nm were selected. and (Ar 80% – O_2 20%), the emission lines at 307.77, 369.1, 753.9, 763.03 nm were used. In the case of pure argon plasma (Ar 100%), several Ar I and Ar II emission lines within the wavelength range of 284.53–842.54 nm were selected. The wavelengths, transition probabilities (Aki), statistical weights (gi), and upper energy levels (Ej) were obtained from the NIST atomic spectra database. A linear regression fitting procedure was applied to the Boltzmann plots to determine the slope of the fitted line, from which the electron temperature was calculated. The quality of the fitting was evaluated using the correlation coefficient (R^2), with values ranging from 0.6433 to 0.9675 for the investigated plasma conditions. the electron temperature is estimated using a Boltzmann plot by plotting $ln\left(I_{ji}\lambda_{ji}/h\ C\ A_{ji}\ g_j\right)$ against the upper energy level Ej. The statistical factor representing the accuracy of the linear fit is indicated by the correlation lines (R^2).

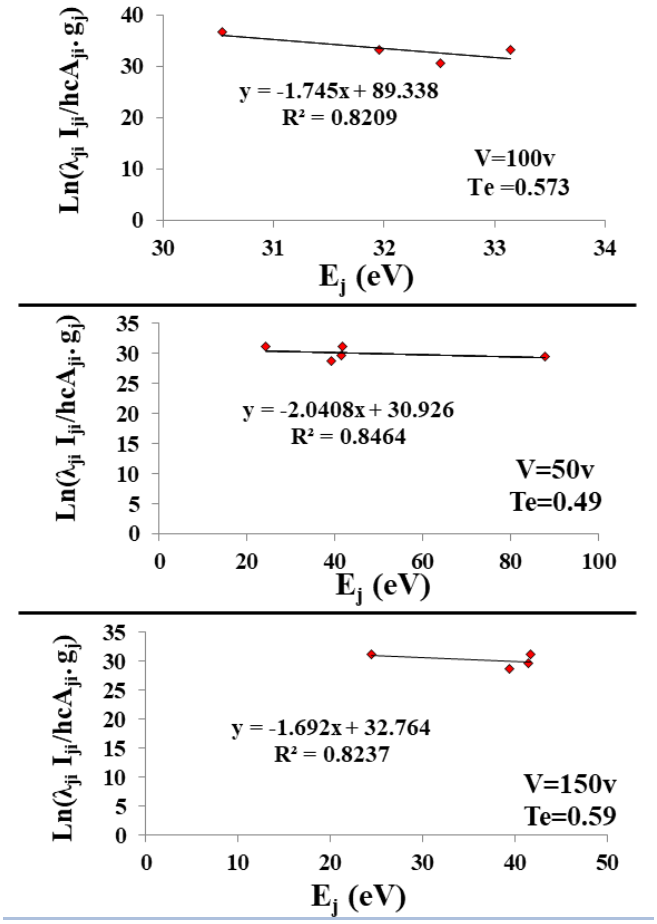


Figure 3. Boltzmann plot for (Microwave plasma) at different potential discharges (50, 100, and 150 volt) for (Ar 20% and O 80%).

The mechanism of electron heating in plasma mainly depends on the energy balance between what electrons gain from the microwave field and what they lose during collisions. When the argon ratio is 100%, the electron temperature is at its highest because argon is an inert gas and does not lose much of its energy (since there are no molecular vibrations), so the electron temperature is high, and it reaches its maximum voltage at (4.2eV). When a fraction of oxygen 20% is mixed with argon, the electron temperature begins to decrease. This is because oxygen is a diatomic molecule and has multiple energy loss channels, such as vibrational excitation, rotational, and dissociation processes and it reaches its maximum voltage to (2.16 eV).

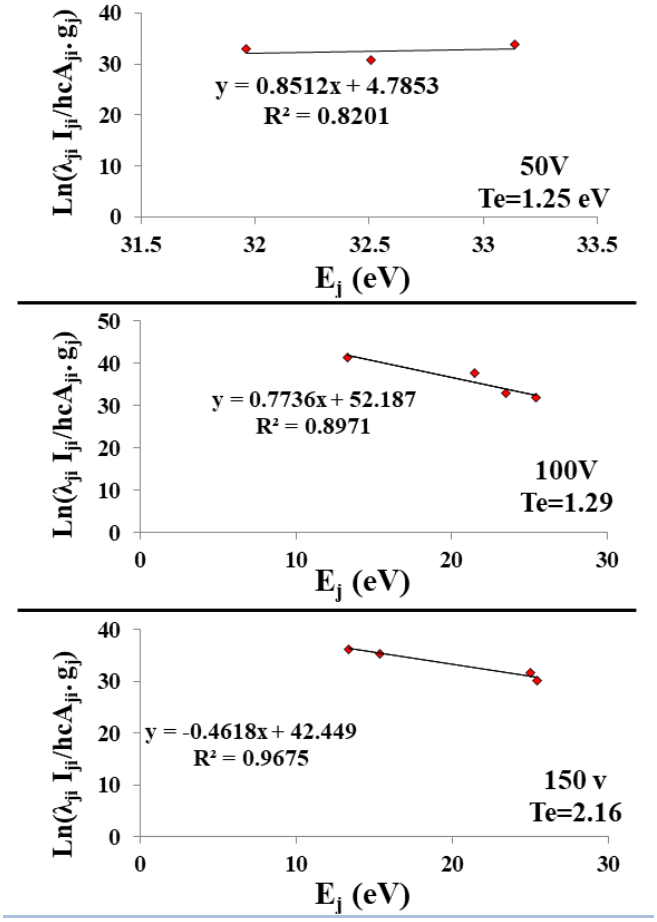


Figure 4. Boltzmann plot for (Microwave plasma) at different potential discharges (50, 100, and 150 volt) for (Ar 80% and O 20%).

These processes consume electron energy efficiently, reducing their average speed and thus lowering the electron temperature. Argon heats the electrons through elastic collisions, while oxygen extracts part of the energy through inelastic processes due to its high electronegativity. When the oxygen concentration is increased to 80%, the electron temperature becomes lower because most of the electron energy is consumed in dissociation and excitation processes, in addition to the phenomenon of electron attachment in oxygen, where electrons are captured, and negative ions are formed, which reduces the number of free electrons and

Downloaded from https://nanomatimp.uomustansiriyah.edu.iq/

Copyright © 2026. This work licensed under a Creative Commons Attribution Noncommercial 4.0 International License.

weakens their ability to gain energy from the field and it reaches its maximum voltage at (0.59 eV).

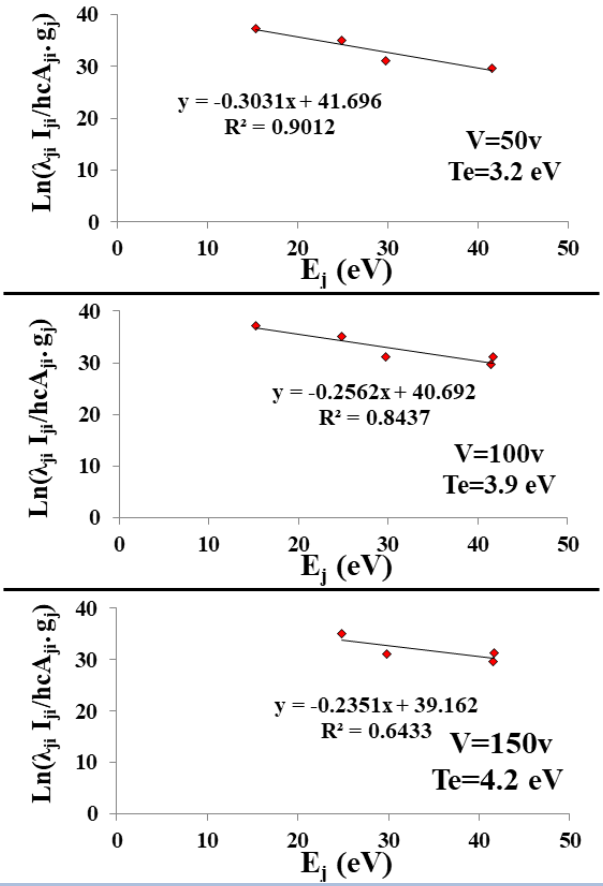


Figure 5. Boltzmann plot for (Microwave plasma) at different potential discharges (50, 100, and 150 volt) for (Ar 100%).

When the oxygen percentage is 80%, as shown in **Table 4**, it works on withdrawing electrons ($O_2 + e^- \rightarrow O_2^-$), causing the direct free electrons to decrease and, negative ions to form, which reduces the electron temperature and decreases ionization, while the density remains low.

Table 5 illustrate the electron density reduces when a mixture of 80% argon and 20% oxygen is used because oxygen is an electronegative gas that tends to capture free electrons and convert them into negative ions. This leads to a reduction in the number of free electrons in the plasma. Additionally, the presence of oxygen causes the loss of electron energy in processes such as excitation and dissociation instead of ionization, and thus the production of new electrons decreases.

In the case of argon 100%, as shown in the **Table 6**, we find that the density gradually begins to decrease because argon is well ionized at the beginning according to equation ($Ar + e^- \rightarrow Ar^+ + 2e^-$), where the electrons are lost through diffusion and there are no (primary or secondary) reactions supporting the increase of electrons. Therefore, the density decreases (12.3 to 9.9 ×1017 cm-3) with the increase of voltage.

Table 4. Plasma parameters of Zn foil for (Microwave plasma) at different potentials (50, 100, and 150 volt) for Ar 20% and O 80%).

V (volt)	T_e (eV)	$n_e \times 10^{17}$ (cm^{-3})	$f_p \times 10^{12}$ (Hz)	$\lambda_D \times 10^{-5}$ (cm)	$N_d \times 10^3$
50	0.490	12.00	9.837	0.475	0.538
100	0.570	9.32	8.670	0.579	0.757
150	0.590	9.26	8.639	0.591	0.800

Table 5. Plasma parameters of Zn foil for (Microwave plasma) at different potentials (50, 100, and 150 volt) for Ar 800% and O 20%).

V (volt)	T_e (eV)	$n_e \times 10^{17}$ (cm^{-3})	$f_p \times 10^{12}$ (Hz)	$\lambda_D \times 10^{-5}$ (cm)	$N_d \times 10^3$
50	1.250	7.50	7.777	0.959	2.773
100	1.290	8.25	8.156	0.925	3.738
150	2.160	8.40	8.230	1.187	5.879

Table 6. Plasma parameters of Zn foil for (Microwave plasma) at different potentials (50, 100, and 150 volt) for Ar100% and O 0%).

V (volt)	T_e (eV)	$n_e \times 10^{17}$ (cm^{-3})	$f_p \times 10^{12}$ (Hz)	$\lambda_D \times 10^{-5}$ (cm)	$N_d \times 10^3$
50	3.200	12.30	9.959	1.198	8.868
100	3.900	10.20	9.069	1.447	12.944
150	4.200	9.90	8.935	1.524	14.684

The relationship between density and electron temperature as a function of voltage can be translated through **Figure 6**.

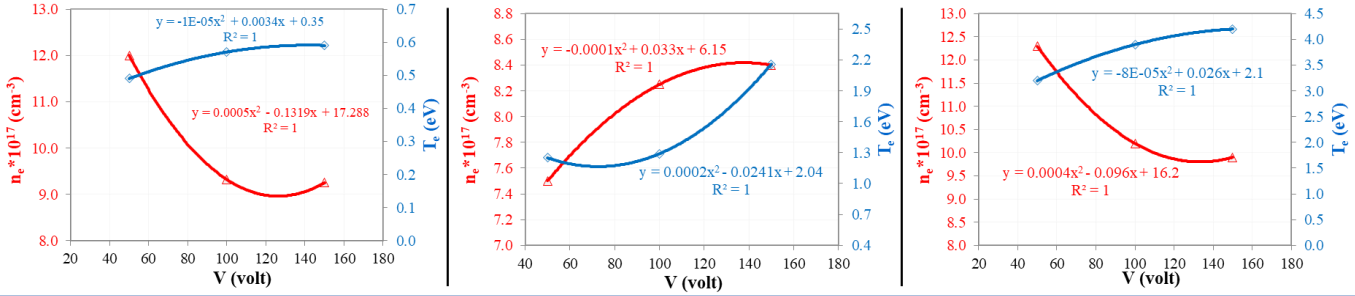


Figure 6. Variation of (T_e) and (n_e) versus the potential discharges (50, 100, and 150) Volt using Microwave plasma technique.

Downloaded from https://nanomatimp.uomustansiriyah.edu.iq/

Copyright © 2026. This work licensed under a Creative Commons Attribution Noncommercial 4.0 International License.

X-ray diffraction (XRD)

X-ray diffraction (XRD) patterns for the (ZnO/Zn) surface on zinc sheets were prepared using microwave plasma at different applied voltages (50, 100, and 150 V). **Figure 7** shows the XRD pattern of the Zn surface with an Ar/O mixture ratio of (20%-80%). Diffraction peaks were observed at 2θ = 36.3°, 38.8°, 43.2°, 54.3°, and 70.2° Since Miller's indices for these angles are as follows (101), (100), (101), (102) and (230) respectively.

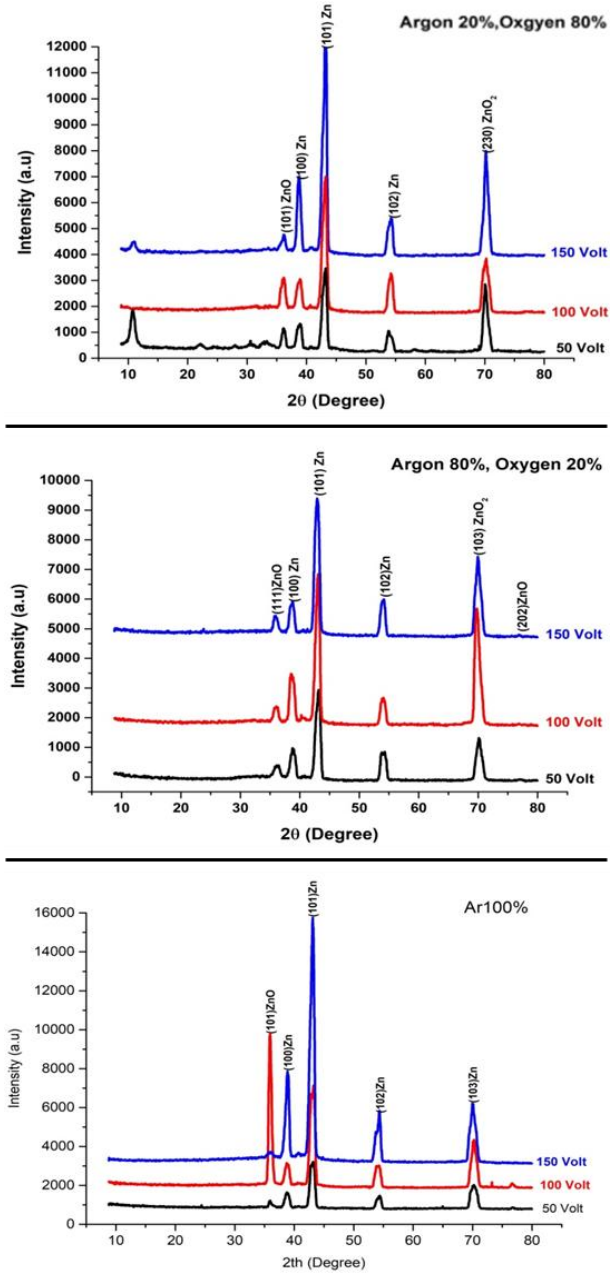


Figure 7. XRD patterns of ZnO foil using microwave plasma technique for different voltage (50, 100, and 150) at (20 l/min) flow gas and constant exposure time 30 sec.

Figure 7 (Ar / O - 80% / 20%) appearance diffraction peaks were observed at 2θ = 35.8°, 38.8°, 53.8°, and 70.07°, Miller's indices for these angles (111), (100), (101, (102), (103) and (202). The peaks remained constant despite the increase in voltage, with only a slight increase in current. At ratio Ar 100% as shows in figure 7, the XRD appeared different angles was observed at 2θ = (35.7°, 38.9°, 43.1°, 54.3°, and 69.9°), and the peak positions changed to (101), (100), (101), (102), and (103). This is consistent with JCPDS (04-0831) and JCPDS (36-1451). From the figures, we observe that as the voltage increases, a slight peak creep occurs, accompanied by oxidation; subsequently, the peaks return to their original positions. We also observe that the highest diffraction pattern between (40° and 50°) indicates the formation of a closely packed hexagonal structure (hcp) of zinc and the wurtzite structure of ZnO. The change in the crystal phase with increasing applied voltage and gas ratios is attributed to the high energy of active particles that interact with the surface, which led to the rearrangement of atoms and the enhancement of phase transitions on the zinc surface. Furthermore, the increased plasma intensity contributed to the enhancement of oxidation and crystallization processes, which was reflected in the appearance and disappearance of some diffraction peaks in the X-ray diffraction patterns. These results indicate success in forming the nanostructure according to X-ray diffraction (XRD) analysis[64, 65]. Figures show a difference in the peaks due to the variation in gas ratios.

Field Emission Scanning Electron Microscopy (FE-SEM) Analysis

Figure 8 shows images of the surface of zinc metal after microwave plasma treatment. Figure A illustrates the changes in surface morphology after exposure to plasma resulting from an (argon/oxygen) mixture at a ratio of (80%-20%), which clearly affected the surface and altered its properties. An increase in voltage leads to changes in surface features, and noticeable modifications began to appear due to the effectiveness of argon gas, as well as the smoothness provided by oxygen to the surface. Cracks and aggregations of nanoparticles were observed in a series of spherical grains. At a voltage of 150 volts, the ion bombardment rate increases, leading to the removal of surface impurities and the creation of slight roughness. Differences in gray levels also reflect changes in the backscattered charge density due to variations in the thickness of the formed oxides.

When the (argon/oxygen) gas mixture ratio was changed to (20%-80%), the increase in oxygen content clearly affected the zinc surface by improving its nanostructure. From all figures, nano-grain agglomerates of heterogeneous sizes appear alongside smooth regions. Additionally, bright areas reveal nano-agglomerates of zinc oxide ZnO. Resulting from the rapid oxidation of zinc and the rearrangement of atoms into a flower-like shape. The small particles (~20–80 nm) approximately represent the nuclei that

When changing the (argon) gas concentration (100%) At 50 volts, the surface exhibits a fine-grained morphology with relatively small and uniform nanoclusters, indicating an ionic effect that leads to moderate surface activation. Increasing the voltage to 100 volts results in a noticeably rougher structure, accompanied by larger nanocluster formations, reflecting enhanced ion bombardment that facilitates atomic

Downloaded from https://nanomatimp.uomustansiriyah.edu.iq/

Copyright © 2026. This work licensed under a Creative Commons Attribution Noncommercial 4.0 International License.

rearrangement and moderate grain growth. At 150 volts, the surface develops more complex and distinct nanostructures characterized by larger hemispherical clusters and deeper gaps between the aggregations, indicating a stronger plasma-surface interaction. Overall, the results confirm that adjusting the microwave plasma voltage provides precise control, and the particle size demonstrates the plasma voltage's capacity to effectively tailor the nanoscale surface structure.

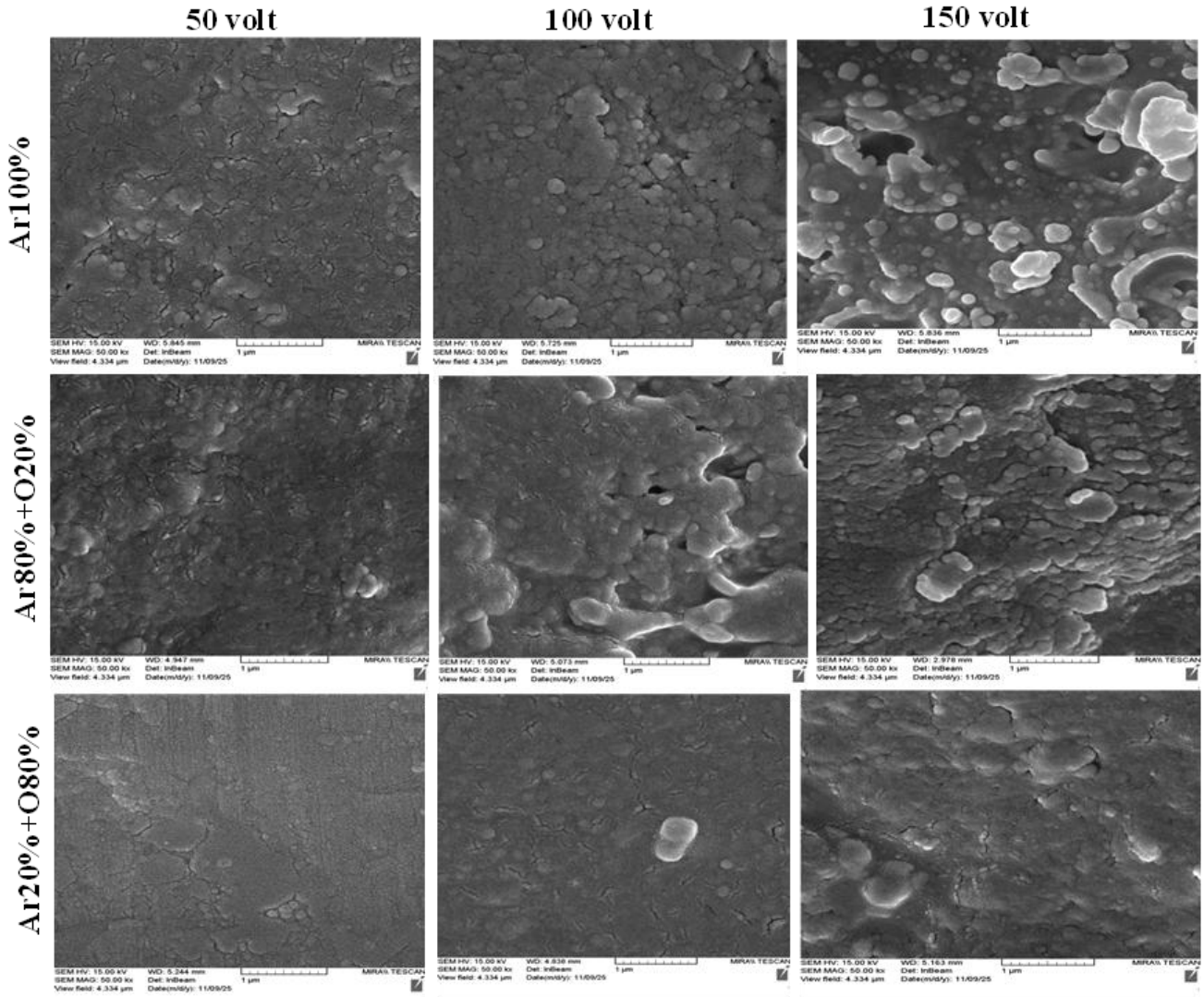


Figure 8. illustrates the effect of argon-oxygen gas ratios on the surface of zinc metal and the effect of electron temperature on etching at three voltages (50, 100, 150 volt) using microwave plasma technology.

Conclusion

The conclusions regarding the effect of gas mixtures on zinc surface etching can be summarized as follows:

The etching behavior on zinc surfaces directly depends on the ratio of argon to oxygen, which determines the balance between physical (ionization) and chemical (oxidation) processes. In pure argon, ion scattering dominates, leading to strong etching and direct removal of zinc without forming compounds. When oxygen is added in specific ratios, a balance between excitation and oxidation is achieved, resulting in surface modification and the formation of a thin zinc oxide layer, with limited ongoing etching. At higher oxygen levels, chemical reactions dominate, forming a dense zinc oxide layer, which reduces the etching rate and acts as a protective layer. The XRD results indicate that the dominant phase in the prepared samples is metallic Zn with a hexagonal structure. The absence or weak intensity of ZnO-related peaks suggests that the surface oxide layer is significantly reduced or modified during the microwave plasma treatment. This behavior can be explained by the high-energy plasma environment, which promotes surface activation and crystallite reorganization, with possible partial removal of the native surface oxide layers. In addition, the variation in peak intensities reflects changes in crystallographic orientation and surface structure induced by the plasma processing conditions. Generally, surface roughness and properties can be controlled by varying the gas ratios. Argon induces physical etching, while oxygen results in chemical surface modification.

Downloaded from https://nanomatimp.uomustansiriyah.edu.iq/

Copyright © 2026. This work licensed under a Creative Commons Attribution Noncommercial 4.0 International License.

Acknowledgment

The authors acknowledge the Department of Physics, College of Science, Mustansiriyah University, Baghdad, Iraq, for their support of this project.

Statement on Data Availability

All data, including any supplementary files, supporting the study's conclusions, are incorporated within the paper.

Declaration of Competing Interests

The authors would like to confirm that there is no conflict of interest accompanying this article.

Funding

There has been no financial support for this work that could have influenced its outcome. Also, both authors confirm that no funding was already received for achieving this work

Author contribution

Baida M. Ahmed proposed the work idea, drafted the plans, and wrote the main manuscript. Heba G. Akhlefa, on the other hand, interpreted the results. All researchers reviewed the final version of the article.

References

[1] I. V. Krivtsun, L. Golovko, S. Fomichov, O. Kaglyak, and Y. Chvertko, "Physical Phenomenon of Laser, Arc, Plasma and Hybrid Laser-Plasma Processes," *Laser and Hybrid Technologies for Surface Engineering and Welding*, 2026.

https://doi.org/10.1007/978-3-032-15038-7_1.

[2] B. M. Ahmed, K. A. Ahmed, and R. K. Ahmed, "Energy loss of correlated ions in dense plasma," *Electronic Materials Letters*, vol. 12, no. 3, p. 419–424, 2016.

https://doi.org/10.1007/s13391-015-5251-2.

[3] A. A. A. Sari *et al.*, "An effective procedure used metal-organic framework for determination of cadmium ions in real tap water and human blood plasma samples," *Spectrochim Acta A Mol Biomol Spectrosc*, vol. 324, p. 124989, 2025.

https://doi.org/10.1016/j.saa.2024.124989.

[4] M. Yuan *et al.*, "Programmable Electromagnetic Wave Absorption via Tailored Metal Single Atom-Support Interactions," *Adv Mater*, vol. 37, no. 8, p. e2417580, 2025.

https://doi.org/10.1002/adma.202417580.

[5] E. Sucu and İ. Sakallı, "Dynamics of particles surrounding a stationary, spherically-symmetric black hole with Nonlinear Electrodynamics," *Physics of the Dark Universe*, vol. 47, p. 101771, 2025.

https://doi.org/10.1016/j.dark.2024.101771.

[6] B. Wang and Y. Lu, "Multi - dimensional micro/nanorobots with collective behaviors," *SmartMat*, vol. 5, no. 5, p. e1158, 2024.

https://doi.org/10.1002/smm2.1263.

[7] A. I. Kravchenko, A. I. Zhukov, and O. A. Datsenko, "Temperature Dependences of the Peclet Number in Sublimation Processes of Simple Substances," *Problems of Atomic Science and Technology*, no. 1, p. 13–16, 2022.

https://doi.org/10.46813/2022-137-013.

[8] F. Fan *et al.*, "Decoupling analysis between the gas formation and solid-to-liquid transition using an in-situ heating-stage microscopy in the sintering process of high-strength ceramsite from coal-based solid waste," *Construction and Building Materials*, vol. 476, 2025.

https://doi.org/10.1016/j.conbuildmat.2025.141266.

[9] T. Matthews *et al.*, "Mortality impacts of the most extreme heat events," *Nature Reviews Earth & Environment*, vol. 6, no. 3, p. 193–210, 2025.

https://doi.org/10.1038/s43017-024-00635-w.

[10] G. Liao *et al.*, "The Evolution of Secondary/Extractive Electrospray Ionization: From Ionization Mechanism to Instrumental Advances," *Mass Spectrom Rev*, vol. 45, no. 2, p. 334–360, 2026.

https://doi.org/10.1002/mas.21931.

[11] T. Yazdani Motlagh *et al.*, "A combined numerical and experimental study of the formation of powder particles from precursor droplets in a plasma flow field," *Powder Technology*, vol. 468, 2026.

https://doi.org/10.1016/j.powtec.2025.121610.

[12] Z. Lv, S. Xie, Y. Li, M. S. Hossain, and A. El Saddik, "Building the metaverse using digital twins at all scales,states, and relations," *Virtual Reality & Intelligent Hardware*, vol. 4, no. 6, p. 459–470, 2022.

https://doi.org/10.1016/j.vrih.2022.06.005.

[13] H. Ruan, T. Xia, and Y. Wang, "Investigation of flashover occurrence criterion based on thermal equilibrium theory," *Journal of Building Engineering*, vol. 92, p. 109658, 2024.

https://doi.org/10.1016/j.jobe.2024.109658.

[14] M. I. Boulos, P. L. Fauchais, and E. Pfender, "Thermodynamic Properties of Plasmas," in *Handbook of Thermal Plasmas*, 2023, pp. 211–256.

https://doi.org/10.1007/978-3-030-84936-8_6.

[15] W. Zhao *et al.*, "Non-thermal plasma and modified catalysts: A synergistic approach to air purification," *Chemical Engineering Journal Advances*, vol. 22, p. 100748, 2025.

https://doi.org/10.1016/j.ceja.2025.100748.

[16] A. Smirnov, Y. Shprits, H. Lühr, and et al., "Extreme two-phase change of the ionospheric electron temperature overshoot during geomagnetic storms uncovered by neural networks," in *EGU General Assembly 2025*, 2025.

https://doi.org/10.5194/egusphere-egu25-19863.

[17] F. Yang, X. Song, and Z. Yu, "Adaptive mode selection of electrical activities in a neuron with a memristive ion

Downloaded from https://nanomatimp.uomustansiriyah.edu.iq/

Copyright © 2026. This work licensed under a Creative Commons Attribution Noncommercial 4.0 International License.

channel," *Nonlinear Dynamics*, vol. 113, no. 7, p. 7213–7222, 2024.

https://doi.org/10.1007/s11071-024-10710-y.

[18] M. Petkova *et al.*, "Cellular responses to prolonged non-thermal plasma exposure in Schizosaccharomyces pombe," *Appl Microbiol Biotechnol*, vol. 110, no. 1, p. 102, 2026.

https://doi.org/10.1007/s00253-026-13786-1.

[19] M. Mozetič, "Low-pressure non-equilibrium plasma technologies: scientific background and technological challenges," *Reviews of Modern Plasma Physics*, vol. 9, no. 1, p. 25, 2025.

https://doi.org/10.1007/s41614-025-00201-x.

[20] W. B. Abdalmuhdi, M. F. H. Al-Kadhemy, K. N. Abbas, and A. A. Saeed, "Thermal effects on the optical behavior and sensitivity of Rh6G-F/PVA composite films," *Journal of Materials Science: Materials in Electronics*, vol. 37, no. 1, 2025.

https://doi.org/10.1007/s10854-025-16435-x.

[21] E. Hanan *et al.*, "Exploring the impact of atmospheric cold plasma technology on plant-based milk analogues and their proteins: A review," *Food Chem X*, vol. 34, p. 103519, 2026.

https://doi.org/10.1016/j.fochx.2026.103519.

[22] G. W. Yang *et al.*, "Atmospheric-pressure microwave plasma torch for energy-efficient NOx generation and direct production of high-concentration plasma-activated water for on-site fertilizer," *Chemical Engineering Journal Advances*, vol. 26, 2026.

https://doi.org/10.1016/j.ceja.2026.101063.

[23] Y. Zhang, X. Wang, Y. Zeng, Q. Hao, S. Wang, and Z. Huang, "Innovative Strategies for Enhancing Heating Uniformity and Quality in Radio Frequency Food Processing: Challenges and Future Directions," *Food Engineering Reviews*, vol. 17, no. 3, p. 756–775, 2025.

https://doi.org/10.1007/s12393-025-09410-z.

[24] C. Li *et al.*, "Plasma‐assisted fabrication of multiscale materials for electrochemical energy conversion and storage," *Carbon Energy*, vol. 7, no. 2, p. e641, 2024.

https://doi.org/10.1002/cey2.641.

[25] M. Hori, "Radical-controlled plasma processes," *Reviews of Modern Plasma Physics*, vol. 6, no. 1, p. 36, 2022.

https://doi.org/10.1007/s41614-022-00084-2.

[26] J. Yu *et al.*, "Stack pressure-A critical strategy and challenge in performance optimization of solid state batteries," *Energy Storage Materials*, vol. 76, p. 104134, 2025.

https://doi.org/10.1016/j.ensm.2025.104134.

[27] M. E. A. Ben Seghier, D. Höche, and M. Zheludkevich, "Prediction of the internal corrosion rate for oil and gas pipeline: Implementation of ensemble learning techniques," *Journal of Natural Gas Science and Engineering*, vol. 99, p. 104425, 2022.

https://doi.org/10.1016/j.jngse.2022.104425.

[28] M. G. Jasim and H. R. Humud, "Reactive Species and Storage Stability of Plasma-Activated Water from Ar + N_2 and Ar + O_2 DBD Systems," *Plasma Chemistry and Plasma Processing*, vol. 46, no. 1, 2025.

https://doi.org/10.1007/s11090-025-10626-4.

[29] M. Imran, N. U. Rehman, and N. Wali, "Effect of pressure and current density on metastable argon dynamics in low-pressure Ar-O2 plasma," *Physica Scripta*, vol. 100, no. 2, p. 025606, 2025.

https://doi.org/10.1088/1402-4896/ada315.

[30] A. Ganjovi, G. Speranza, G. Gottardi, M. Testi, L. Crema, and R. Bartali, "Energy redistribution under argon dilution in a low-pressure methane RF plasma," *Physics of Plasmas*, vol. 33, no. 2, p. 023514, 2026.

https://doi.org/10.1063/5.0305798.

[31] S. K. Soe *et al.*, "A New Insight into Balancing Reactive Oxygen Species in Piezodynamic Therapy," *Advanced Functional Materials*, vol. 36, no. 7, 2025.

https://doi.org/10.1002/adfm.202513106.

[32] D. Yang *et al.*, "Surface-Enhanced Raman Spectroscopy for the Detection of Reactive Oxygen Species," *ACS Nano*, vol. 19, no. 2, p. 2013–2028, 2025.

https://doi.org/10.1021/acsnano.4c15509.

[33] R. Q. Mohammed and B. M. Ahmed, "Enhanced Nonenzymatic Glucose Biosensor of ZnO Nanostructure via Nonthermal Plasma," *International Journal of Nanoscience*, vol. 23, no. 6, p. 2450018–361, 2024.

https://doi.org/10.1142/S0219581X24500182.

[34] Z. Zhang, Y. Wang, T. Guo, and P. Hu, "The Influence of Defect Engineering on the Electronic Structure of Active Centers on the Catalyst Surface," *Catalysts*, vol. 15, no. 7, p. 651, 2025.

https://doi.org/10.3390/catal15070651.

[35] S. Tao *et al.*, "A Smart Catalytic System with In Situ Dynamic Current‐Tuned Pd‐Ce Diatomic Interactions for Enhanced Methane Oxidation," *Advanced Functional Materials*, vol. 36, no. 18, 2025.

https://doi.org/10.1002/adfm.202519202.

[36] Y. Li *et al.*, "Capacitance-Enhanced Battery: Integrating High-Density Battery Capacity with Supercapacitive Swiftness in an Ultra-Large MXene Architecture," *Adv Mater*, vol. 37, no. 42, p. e08336, 2025.

https://doi.org/10.1002/adma.202508336.

[37] S. Feng *et al.*, "Argon anodic plasma inert anode for Low-Temperature aluminium electrolysis," *Chemical Engineering Journal*, vol. 472, p. 145010, 2023.

https://doi.org/10.1016/j.cej.2023.145010.

[38] B. M. Ahmed, M. F. Sultan, A. K. Hasan, and S. M. Ahmad, "Ions energy loss measurements in low and high temperature plasma," *IOP Conference Series: Materials Science and Engineering*, vol. 928, no. 7, p. 072094, 2020.

https://doi.org/10.1088/1757-899x/928/7/072094.

Downloaded from https://nanomatimp.uomustansiriyah.edu.iq/

Copyright © 2026. This work licensed under a Creative Commons Attribution Noncommercial 4.0 International License.

[39] Y. Taneja, D. Dube, and R. Singh, "Recent advances in elemental doping and simulation techniques: improving structural, photophysical and electronic properties of titanium dioxide," *Journal of Materials Chemistry C*, vol. 12, no. 37, p. 14774–14808, 2024.

https://doi.org/10.1039/d4tc02031f.

[40] M. Tan *et al.*, "Amorphous Nanomaterials: Emerging Catalysts for Electrochemical Carbon Dioxide Reduction," *Advanced Energy Materials*, vol. 14, no. 40, p. 2402424, 2024.

https://doi.org/10.1002/aenm.202402424.

[41] L. Han *et al.*, "Multifunctional high-entropy materials," *Nature Reviews Materials*, vol. 9, no. 12, p. 846–865, 2024.

https://doi.org/10.1038/s41578-024-00720-y.

[42] J. Zhou, T. Wei, and X. An, "Combining non-thermal plasma technology with photocatalysis: a critical review," *Phys Chem Chem Phys*, vol. 25, no. 3, p. 1538–1545, 2023.

https://doi.org/10.1039/d2cp04836a.

[43] M. F. Hadi, E. M. Alwaan, and W. H. Abass, "Nonlinear Optical Characteristics of Crystal VioletDye Doped Polystyrene Films by Using Z-Scan Technique," *Al-Mustansiriyah Journal of Science*, vol. 27, no. 5, p. 83–88, 2017.

https://doi.org/10.23851/mjs.v27i5.172.

[44] A. Fattah ‐ alhosseini, A. Fardosi, A. Askari, M. Karbasi, B. Dikici, and M. Kaseem, "Enhancing Plasma Electrolytic Oxidation (PEO) Coatings on Magnesium Alloys: The Critical Role of Surface Pretreatments," *Advanced Materials Interfaces*, vol. 12, no. 14, 2025.

https://doi.org/10.1002/admi.202500192.

[45] D. Kumar, S. Idapalapati, W. Wang, and S. Narasimalu, "Effect of Surface Mechanical Treatments on the Microstructure-Property-Performance of Engineering Alloys," *Materials (Basel)*, vol. 12, no. 16, p. 2503, 2019.

https://doi.org/10.3390/ma12162503.

[46] R. A. S. A. Alkareem and B. M. Ahmed, "Influence of laser energy on optical emission spectroscopy characteristics for zinc plasma parameters," *Journal of Optics*, vol. 55, no. 4, p. 3920–3925, 2025.

https://doi.org/10.1007/s12596-025-02472-6.

[47] I. K. Abbas and K. A. Aadim, "Spectroscopic Diagnosis of Cobalt Plasma Produced by OES Technique and Influence of Applied Voltage on Plasma Parameters," *Iraqi Journal of Science*, vol. 64, no. 5, p. 2271–2281, 2023.

https://doi.org/10.24996/ijs.2023.64.5.15.

[48] A. P. Dhinakaran, P. Vinothkumar, T. S. Senthil, and S. Kalpana, "Investigation on luminescent characteristics of Tb3+/Dy3+co-doped boro-phosphate glass for cool white LED and radiation shielding applications," *Applied Physics A*, vol. 130, no. 10, p. 709, 2024.

https://doi.org/10.1007/s00339-024-07788-x.

[49] A. Khumaeni, W. S. Budi, R. Hedwig, M. A. Gondal, and K. H. Kurniawan, "Signal Intensity Augmentation of Elements Detected in Blood Serum Using Dual Pulse Laser Induced Plasma Spectroscopy Under Ambient He Gas Environment," *Arabian Journal for Science and Engineering*, vol. 49, no. 1, p. 1297–1308, 2023.

https://doi.org/10.1007/s13369-023-08447-8.

[50] L. Lefferts, "Leveraging Expertise in Thermal Catalysis to Understand Plasma Catalysis," *Angewandte Chemie*, vol. 136, no. 10, p. e202305322, 2024.

https://doi.org/10.1002/ange.202305322.

[51] Y. Wu *et al.*, "Excitation-Dependent Anti-Thermal Quenching in Zero-Dimensional Manganese Bromides for Photoluminescence and X-Ray Scintillation," *Angewandte Chemie*, vol. 137, no. 5, p. e202417018, 2025.

https://doi.org/10.1002/ange.202417018.

[52] S. Rath and S. Kar, "Microwave atmospheric pressure plasma jet: A review," *Contributions to Plasma Physics*, vol. 65, no. 2, p. e202400036, 2024.

https://doi.org/10.1002/ctpp.202400036.

[53] T. Yamada and W. Shinoda, "Asymmetry and heterogeneity in the plasma membrane," *Biophys J*, vol. 125, no. 2, p. 387–395, 2026.

https://doi.org/10.1016/j.bpj.2025.06.026.

[54] B. A. Z. Z. M. Abood and A. A. Khadayeir, "Measurement of Electron Temperature (Te) and Electron Density (Ne) Cold Plasma Jets Optical Emission Spectroscopy (OES) Method," *Mustansiriyah Journal of Pure and Applied Sciences*, vol. 2, no. 2, p. 126–133, 2024.

https://doi.org/10.47831/mjpas.v2i2.175.

[55] V. Bende, P. Srikar, R. K. Gangwar, R. L. Bhardwaj, and R. Kar, "A semi-empirical approach to Boltzmann plot analysis for cold atmospheric pressure plasma: Comparison with collision-radiative modelling," *Vacuum*, vol. 249, 2026.

https://doi.org/10.1016/j.vacuum.2026.115263.

[56] A. Bacławski and A. Bartecka, "Experimental and theoretical investigations of the Stark width and shift of the He I 388.865 nm spectral line," *Journal of Quantitative Spectroscopy and Radiative Transfer*, vol. 317, p. 108927, 2024.

https://doi.org/10.1016/j.jqsrt.2024.108927.

[57] M. M. Kadhim and B. M. Ahmed, "Antibacterial Activity of Silver Nanoparticles and Cinnamon Bark Extract Prepared by Pulse Laser Ablation and Plasma Jet Methods," (in en), *Journal of Nanostructures*, vol. 12, no. 3, p. 633–641, 2022.

https://doi.org/10.22052/JNS.2022.03.017.

[58] D. Pal and S. Neogi, "Enhancement of Adhesion of Polymers by Plasma Treatment," in *Progress in Adhesion and Adhesives*, vol. 9, 2025, pp. 65–108.

https://doi.org/10.1002/9781394315086.ch3.

Downloaded from https://nanomatimp.uomustansiriyah.edu.iq/

Copyright © 2026. This work licensed under a Creative Commons Attribution Noncommercial 4.0 International License.

[59] L. Robles-Gómez, P. Sáez-Espinosa, and M. J. Gómez-Torres, "Field Emission Scanning Electron Microscopy (FE-SEM) as an Approach for Membrane Surface Mapping in Cell Biology," in *Spermatology: Methods and Protocols*, M. Álvarez-Rodríguez, Ed. New York, NY: Springer US, 2025, pp. 435–444.

https://doi.org/10.1007/978-1-0716-4406-5_28.

[60] A. Qu, Y. Chen, N. Zhang, and L. Wu, "Design of an adjustable low-temperature linear microwave plasma source for atmospheric pressure applications," *Physics of Plasmas*, vol. 32, no. 1, p. 013502, 2025.

https://doi.org/10.1063/5.0236387.

[61] H. Sekiguchi, "Evaluation of Non-catalytic Reverse Water-Gas Shift Reaction Using Microwave Discharge Plasma at Atmospheric Pressure," *Plasma Chemistry and Plasma Processing*, vol. 46, no. 3, 2026.

https://doi.org/10.1007/s11090-025-10615-7.

[62] R. S. Sabry, M. A. Abid, B. Muhsen, and W. J. Aziz, "Hydrothermal controllable synthesis to convert ZnO hexagonal nanotubes to hexagonal nanorods and their photocatalytic application," *Journal of Materials Science: Materials in Electronics*, vol. 27, no. 11, p. 11176–11181, 2016.

https://doi.org/10.1007/s10854-016-5236-4.

[63] A. Kramida, Y. Ralchenko, and J. Reader. (2022). *National Institute of Standards and Technology (NIST) Atomic spectra database*.

[64] M. S. Ramachandra Rao and T. Okada, *ZnO Nanocrystals and Allied Materials* (Springer Series in Materials Science). 2014.

https://doi.org/10.1007/978-81-322-1160-0.

[65] M. S. Othman, "Optical Response of GaAs0.75Sb0.25 Nanosheet for Dependent Pressure," *Al-Mustansiriyah Journal of Science*, vol. 31, no. 3, p. 120–125, 2020.

https://doi.org/10.23851/mjs.v31i3.864.

Downloaded from https://nanomatimp.uomustansiriyah.edu.iq/

Copyright © 2026. This work licensed under a Creative Commons Attribution Noncommercial 4.0 International License.